Quantum Beat Photoelectron Imaging Spectroscopy of Xe in the VUV

Ruaridh Forbes
Department of Physics, University of Ottawa, 150 Louis Pasteur, Ottawa, ON, K1N 6N5, Canada and Department of Physics and Astronomy, University College London, Gower Street, London, WC1E 6BT, United Kingdom

Varun Makhija*
Department of Physics, University of Ottawa, 150 Louis Pasteur, Ottawa, ON, K1N 6N5, Canada

Jonathan Underwood
Department of Physics and Astronomy, University College London, Gower Street, London, WC1E 6BT, United Kingdom

Albert Stolow
Department of Physics, University of Ottawa, 150 Louis Pasteur, Ottawa, ON, K1N 6N5, Canada Department of Chemistry, University of Ottawa, 10 Marie Curie, Ottawa, Ontario, K1N 6N5, Canada and National Research Council of Canada, 100 Sussex Drive, Ottawa, Ontario K1A 0R6, Canada

Iain Wilkinson
National Research Council of Canada, 100 Sussex Drive, Ottawa, Ontario K1A 0R6, Canada and Methoden der Materialentwicklung, Helmholtz-Zentrum Berlin für Materialien und Energie GmbH, Hahn-Meitner-Platz 1, 14109 Berlin, Germany

Paul Hockett† and Rune Lausten
National Research Council of Canada, 100 Sussex Drive, Ottawa, Ontario K1A 0R6, Canada

Time-resolved pump-probe measurements of Xe, pumped at 133 nm and probed at 266 nm, are presented. The pump pulse prepared a long-lived hyperfine wavepacket, in the Xe $5p^5(^2P^\circ_{1/2})6s\ ^2[1/2]^\circ_1$ manifold (E =77185 cm^{-1} =9.57 eV). The wavepacket was monitored via single-photon ionization, and photoelectron images measured. The images provide angle- and time-resolved data which, when obtained over a large time-window (900 ps), constitute a precision quantum beat spectroscopy measurement of the hyperfine state splittings. Additionally, analysis of the full photoelectron image stack provides a quantum beat imaging modality, in which the Fourier components of the photoelectron images correlated with specific beat components can be obtained. This may also permit the extraction of isotope-resolved photoelectron images in the frequency domain, in cases where nuclear spins (hence beat components) can be uniquely assigned to specific isotopes (as herein), and also provides phase information. The information content of both raw, and inverted, image stacks is investigated, suggesting the utility of the Fourier analysis methodology in cases where images cannot be inverted.

Publication history

- Original manuscript (Authorea), Feb. 2018.
- arXiv, March 2018.

Supplementary material

OSF project **Quantum Beat Photoelectron Imaging Spectroscopy of Xe in the VUV**, DOI: 10.17605/OSF.IO/DS8MK

* vmakhija@uottawa.ca
† paul.hockett@nrc.ca

I. INTRODUCTION

Quantum beat spectroscopy (QBS) provides a time-domain route to high-resolution spectroscopic measurements [1]. In a standard scheme a narrow wavepacket (few-state superposition) is prepared, time-domain measurements are obtained, and Fourier analysis of the signal provides the high-resolution frequency-domain information sought. More generally, quantum beat spectroscopy can be regarded as a subset of generalized wavepacket methods [2], with the specific requirement that sufficient wavepacket revivals are present in the observed temporal window to provide frequency-domain information. The applicability, and details, for a given case will therefore depend on experimental factors - e.g. time-resolution, wavepacket preparation - and intrinsic systems properties - e.g. density of states, lifetimes [3, 4]. Wavepackets

comprised of fine and hyperfine levels in rare gases and alkali atoms are a notable application of QBS, since the lifetimes and level spacings are concomitant with ns and ps experimental time-scales [1, 5].

In order to obtain time-domain data with good signal to noise, an observable which responds to the wavepacket dynamics is required. In many cases, photoelectron angular distributions (PADs) provide a sufficient observable, which may be much more sensitive to underlying dynamics than photoelectron yields or energy spectra alone. In particular, the PADs are sensitive to the angular momentum couplings in the system; for the case of hyperfine interactions, this sensitivity has been investigated extensively by Berry and co-workers for sodium and lithium, prepared with ns pulses [6–8]. In this pioneering atomic ionization work, PADs were measured (in a plane perpendicular to the light propagation) for different time-delays and pump-probe polarization geometries, and the data obtained was sufficient to allow extraction of the photoionization matrix elements (partial-wave magnitudes and phase shifts), and an effective nuclear spin depolarization parameter, related to the hyperfine coupling. The analysis of the temporal evolution was hindered by both the experimental difficulty of recording PADs, rendering it feasible to record PADs at only a few pump-probe delays, and the fact that the pulse durations were non-negligible compared to the hyperfine precession (i.e. the characteristic time-scale of the coherently prepared hyperfine wavepacket) [7]. Nonetheless, the requisite theory and a detailed physical understanding of the hyperfine interaction was developed (see also refs. [9, 10] for related theory work). Subsequent work by various investigators explored this topic further, for example Bajic *et al.* [11], who investigated angle-resolved multi-photon ionization in Kr and Xe, and Reid *et al.* [12], who explored hyperfine depolarization in NO via time and angle-resolved photoelectron measurements; in both cases the work again highlighted the sensitivity of PADs to hyperfine interactions.

Xenon has two naturally occurring isotopes with non-zero nuclear spin (^{129}Xe ($I = 1/2$), ^{131}Xe ($I = 3/2$)), and the hyperfine level structure has been well-studied in the energy domain at a range of energies with a variety of methods, including fluorescence [13], saturated-amplification [14] and photoionization [15–17]; for a more comprehensive overview see ref. [18]. A range of high (energy) resolution ionization experiments incorporating the preparation of high-n Rydberg states have been performed to probe hyperfine splittings in Rydberg manifolds, including autoionizing regions, and in the cation [19, 20]. Recently, photoion-photoelectron coincidence experiments provided isotopically-resolved (hence I-resolved) PADs from the $(^2P^\circ_{3/2})5d\ ^2[3/2]^\circ_1$ state, following VUV excitation at 10.4 eV (83876 cm^{-1}) [21]; subsequent work included detailed theoretical analysis, and the first determination of the hyperfine couplings in this wavelength range [22].

In this work, broadband femtosecond VUV pulses ($\lambda \approx$133 nm, $E_{h\nu} \approx$9.32 eV =75188 cm^{-1}, $\Delta\lambda \approx$1.7 nm, $\tau \approx$80 fs) were used to coherently prepare hyperfine states in the Xe$(^2P^\circ_{1/2})6s\ ^2[1/2]^\circ_1$ manifold[23] (E =77185 cm^{-1} =9.57 eV, NIST value [24], adapted from ref. [15]), which were subsequently ionized with UV pulses (λ =266.45 nm, $E_{h\nu}$ =4.653 eV =37530 cm^{-1}, $\Delta\lambda$ =3 nm, τ =50 fs). The experimental set-up, and details of the VUV generation are presented in Sect. II. In the experiments, photoelectron images were obtained as a function of VUV-UV delay, over a 900 ps temporal window (Sect. III A). As discussed above, temporal modulations in the PADs provide an observable sensitive to the underlying wavepacket dynamics, and this data constitutes a QBS measurement. Determination of the hyperfine splittings, and coupling constants, from the photoelectron data is discussed in Sect. III B. The data additionally suggests a *quantum beat imaging* methodology, in which beat-frequency resolved photoelectron images, and associated phase information, may be obtained: this is discussed in Sect. III C.

The raw experimental data, data processing scripts, and additional analysis notes to accompany this manuscript can be found online via an OSF repository, see Sect. VI for further details.

II. EXPERIMENT

A. VUV-UV photoelectron imaging

The experimental set-up used for the VUV-UV pump-probe photoelectron velocity-map imaging (VMI) measurements at 133 nm reported herein was almost identical to that previously reported for work using 160 nm radiation [25], and the reader is referred to that work for further details of the experimental apparatus beyond the outline sketched here. A similar VUV-UV pump-probe VMI experimental configuration has also been previously reported by Suzuki (see ref. [26] for a summary); for further general discussion of VUV laser spectroscopies in both time and frequency domain precision spectroscopy experiments see, e.g., ref. [27].

Briefly, the optical chain was initiated by a standard amplified titanium-sapphire laser system (Coherent Legend-Elite Duo), which provided 35 fs pulses at 795 nm at 1 kHz. A 2.5 mJ component of the total laser output, 7.5 mJ, was utilized in the experiments presented here. The beam was placed through a 70:30 beamsplitter to provide the pump and probe arms, respectively. The 1.75 mJ is frequency doubled using a 150 μm Beta Barium Borate (β-BaB_2O_4, β-BBO), to provide 397.5 nm (2ω) pulses with an estimated pulse duration of 40 fs. The 2ω light was then separated from the fundamental by using dielectric mirrors. The 2ω pulses were the focused (ROC = 1.5 m) into an argon-filled gas cell, where the 2ω pulse was frequency tripled by a six-wave mixing process, as described by Trabs and coworkers [28, 29]. The 6ω femtosecond pulse was then separated from the

driving field, and refocused, using 0 deg. reflections from dielectric mirrors centred at 133nm (Layertec GmbH). The optical layout of the VUV generation chamber, and a representative spectrum of the generated radiation, is shown in figure 1. The spectrum was obtained with a VUV spectrometer (Resonance VS7550) in the configuration as shown in fig. 1. The recorded spectrum is uncalibrated, but expected to be centred at $\lambda = 132.5$ nm based on the driving field wavelength, and stable as a function of driving field intensity [28, 29]. Although this is somewhat to the red of the target pump transition to populate states in the $(^2P^\circ_{1/2})6s\ ^2[1/2]^\circ_1$ manifold lying at $E = 77185$ cm^{-1} ($\lambda = 129.6$ nm), significant resonance-enhanced photoelectron signal was observed in the VMI measurements detailed below. This indicates that the wings of the pulse contained sufficient flux to drive the pump transition, and/or a slight blue-shift of the spectrum from the expected central wavelength.

For photoelectron imaging experiments, the VUV spectrometer was replaced with a VMI spectrometer [30], separated from the VUV generation chamber by a minimal thickness (0.5 mm) CaF_2 window (Crystran). For pump-probe measurements, the remaining 0.75mJ of the fundamental transmitted through the beamsplitter was delayed using a motorized stage (Newport XML210), frequency tripled in two β-BBO crystals (see ref. [25] for further details), and then recombined with the 6ω pulse, in a collinear geometry.

The pump and probe beams were focused through a set of baffles, to minimize signals from scattered VUV and UV light, into the interaction region of a VMI spectrometer. An atomic beam of Xe was generated in a separate source chamber by expanding a 7.5% mix of Xe (Praxair Canada Inc., 5N purity) seeded in He (BOC GAZ, 5N purity) through an Even-Lavie valve [31], operating at 1 kHZ and held at 40 ^{o}C, at a pressure of 20 psi (138 kPa). The supersonic expansion was skimmed, yielding an atomic beam with an estimated diameter of $\sim$1 mm, before entering the interaction along the VMI Time-of-Flight (ToF) axis. The VMI spectrometer consisted of a three-stage, open aperture repeller electrode system, and a ten-element Einzel lens stack [25]. Accelerated electrons were detected using an MCP-Phosphor detector setup and photoelectron images recorded by relay-imaging the phosphorescence at a CCD camera (Thorlabs DC210). A cross-correlation of τ_{xc} =170 fs (FWHM) in the interaction region of the VMI spectrometer was determined by resonantly enhanced two-color ionization of xenon. The extended duration of the cross-correlation (as compared to the optimal transform-limited cross-correlation value of ca. 60 fs for these pulses) is attributed primarily to dispersion of the 6ω pulse in the CaF_2 window. In future work, a switch to an LiF window, combined with upstream dispersion compensation, should enable transform-limited 6ω pulses (ca. 40 fs) in the interaction region of the spectrometer.

Time-resolved photoelectron images were recorded for pump-probe delays between t =-70 ps and t =+890 ps in steps of 10 ps. Here, negative delay refers to the situation where the 3ω pulse arrives before the 6ω. The time-resolved photoelectron signals were constructed from the measured photoelectron images in the following manner. At each time-delay of the pump and probe, two photoelectron images where recorded: one with the gas pulse temporally overlapped with the two lase pulses; and one without the gas pulse (to account for ionization due to background contaminant gases and scattered light signals associated with the 6ω pulse). The "no gas" signal was then subtracted from the gas pulse data to obtain background gas and scatter free images. It is of note that no one-color photoelectron counts, bar scatter light signals, were observed with the 6ω pulse. Additionally, negligible counts with 3ω pulse were observed with the pulse energies and MCP/phosphor voltage settings employed during the collection of the images. In total, 25 scans of the pump-probe delay window were performed. Energy to pixel calibration was achieved by recording 3-photon ionization of Xe at 266 nm under the same VMI focusing conditions utilized in the experiment.

B. Data processing

The energy and time-dependent photoelectron distributions can be defined in the usual way, in terms of a spherical harmonic expansion (see, e.g., ref. [32])

$$I(\theta, \phi, E, t) = \sum_{L,M} \beta_{L,M}(E,t) Y_{L,M}(\theta, \phi) \qquad (1)$$

where E is the photoelectron kinetic energy and t the pump-probe delay; $\beta_{L,M}$ are the anisotropy parameters, which can be related to the photoionization dynamics of the system. For cylindrically-symmetric distributions, only $M = 0$ terms are non-zero, and the ϕ coordinate is redundant: this is the case for the measurements reported herein, and these terms are subsequently omitted in this manuscript. For 2D imaging of cylindrically-symmetric 3D distributions, in which the 3D photoelectron distribution is projected onto the detector in the measurements (sometimes termed "crush" imaging), the symmetry of the projection enables 2D slices from the original 3D photoelectron distributions to be reconstructed using standard inversion techniques [33]. To reconstruct the slices, and determine the $\beta_L(E,t)$ metrics, the photoelectron images were processed using cpBasex, which implements the pBasex inversion method [34]. This method uses a fitting methodology, and provides both inverted (or "slice") images, hereafter denoted by the coordinate system (x_i, y_i, t), and the associated $\beta_L(E,t)$ expansion parameters directly. For the distributions considered herein, from a two-photon process with cylindrical symmetry, the only non-zero parameters are $L = 0, 2, 4$. (For non-cylindrically symmetric distributions, e.g. distributions arising from non-parallel pump-probe polarization geometries, direct inversion is not possible, although other methods - for instance tomographic recon-

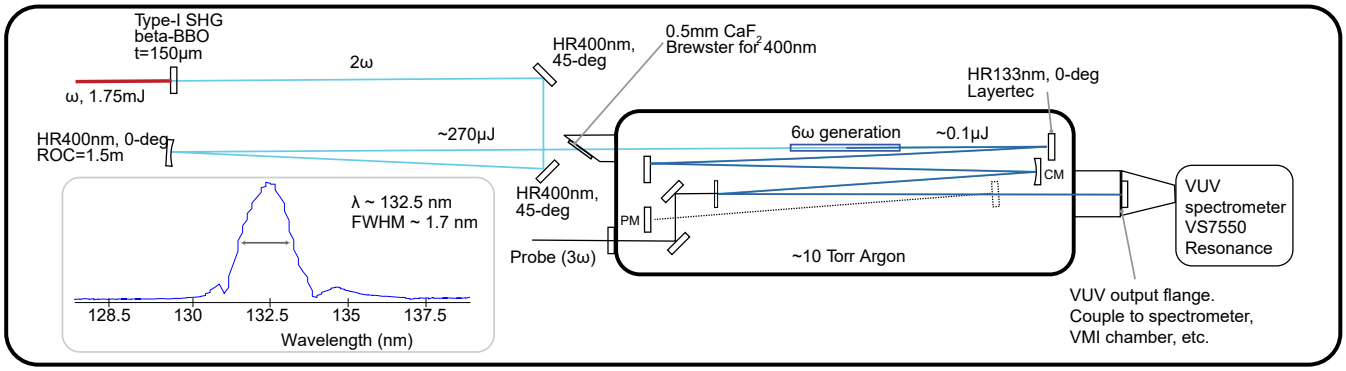

Figure 1. Layout of the 6ω generation chamber, configured to record the VUV spectrum. For photoelectron experiments, the VUV spectrometer was replaced with a VMI spectrometer. HR: high-reflector, CM: curved mirror. Inset shows a typical 6ω spectrum, recorded with a VUV spectrometer (Resonance VS7550, uncalibrated, see main text for details).

struction - can be applied with some additional experimental effort. For further general discussion on charged particle imaging and reconstruction, see ref. [33], for recent discussion in the context of 2D and 3D metrology techniques, including photoelectron tomography, see, for instance, ref. [35] and references therein.)

Images were defined and processed via a variety of analysis protocols, including per-scan and scan-summed, and with and without image symmetrization. The processing of images from each experimental scan provided a way to estimate statistical uncertainties, while scan-summed and symmetrized images provided the best signal-to-noise, hence highest resolution, dataset. Other selections, e.g. summation over a sub-set of the scans, choice of a single quadrant from the photoelectron images, and so forth, provided additional validation and cross-checks on the extracted data. In the results reported herein, the scan-summed dataset was the main focus of the analysis, and statistical (1σ) uncertainties were determined from analysis on a per-scan basis (see also Sect. VI).

III. RESULTS AND DISCUSSION

A. Photoelectron images

Figure 2(a) illustrates typical raw (un-symmetrized) photoelectron imaging results at various pump-probe time delays. The images show a dramatic change in the angular dependence of the outer ring as a function of pump-probe delay, t, with clear switching from a four-lobed to two-lobed structure. At a total photon energy of 14.24 eV (114850 cm $^{-1}$), there is 2.1 eV of excess energy above the first ionization threshold at 12.13 eV (97833 cm^{-1}, values from NIST, ref. [24], adapted from refs. [36, 37]), and two final J^+ states can be populated in the ion:

- $Xe^+(5p^5)^2P^\circ_{3/2}$ (ground state)
- $Xe^+(5p^5)^2P^\circ_{1/2}$ (1.3 eV, 10537 cm $^{-1}$)

The outer photoelectron band (maximum photoelectron energy) in the images is therefore correlated with formation of the cation with $J^+ = 3/2$, while the inner ring correlates with the $J^+ = 1/2$ spin-orbit excited state; the corresponding photoelectron energies (band centres) are E=2.1 eV and E=0.8 eV, respectively. Inverted (slice) images are also shown in Figure 2(b) for reference.

A visualisation of the full (x, y, t) volume is shown in figure 3(a), and the inverted image volume (x_i, y_i, t) in figure 3(b). In these renderings only the top right quadrant of the images is included, and 10 isosurfaces are shown, spaced over 10 - 90% photoelectron yield (normalised to the maximum volume element). The renderings give a sense of the full dataset: temporal oscillations are clearly observed, particularly in the outer photoelectron band, and some aspects of the changing angular distributions can be discerned (this is less apparent in the static renderings, but can be seen more clearly in the interactive versions available online), although are not pronounced.

A more quantitative picture is obtained by analysis of the results in terms of the characteristic $\beta_L(\Delta E, t)$ parameters, as discussed in Sect. II B. Metrics extracted from the processed images over a small energy range ΔE, defined by the FWHM of the photoelectron features, are illustrated in figure 4. It is immediately apparent from the data that the PADs change significantly as a function of pump-probe delay, with clear oscillations apparent in the temporal profiles of $\beta_2(t)$ and $\beta_4(t)$ for both photoelectron bands. The oscillations are not, however, clearly observed in the photoelectron yield (denoted $\beta_0(t)$), which shows a gradual decay with only a hint of the oscillations observed in the $L > 0$ terms. This is due to the strong dependence of the PADs on the evolution of the hyperfine wavepacket as a function of time, while the total yields are much less sensitive [8, 38].

For the inner band ($J^+ = 1/2$), the lower photoelectron yield results in higher noise in the extracted param-

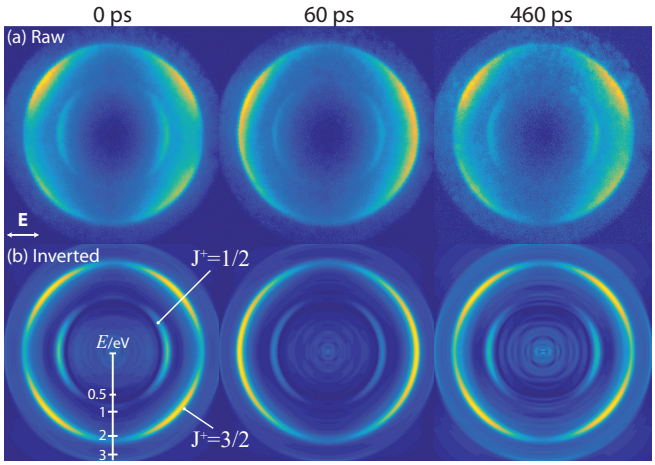

Figure 2. Example photoelectron images. (a) Raw images, summed over experimental cycles. The electric field polarization vector was horizontal, as indicated. (b) The corresponding inverted images. Photoelectron bands are labelled by the final cation states, $J^+ = \frac{1}{2}$ and $J^+ = \frac{3}{2}$, corresponding to electron energies $E = 0.8$ eV and $E = 2.1$ eV respectively. Scale bar shows pixel ($\propto$ velocity) to E conversion. Colour maps were normalised to the maximum signal intensity for each image (arb. units). The differences between quadrants in the raw images, which should be identical by symmetry, is ascribed primarily to detector inhomogeneities, although other experimental factors may also contribute.

eters, but clear quantum beats are still observed. These beats are out-of-phase with the $J^+ = 3/2$ traces. Empirically, this indicates a sign change in the excited state polarization (alignment tensor) sensitivity of the two ionizing transitions. The sign change is consistent with the treatment of Greene and Zare [9], in which a universal alignment function is derived; the sign of this function depends on angular momentum transfer, and changes between $\Delta J = 0$ and $\Delta J = \pm 1$ ionizing transitions. This behaviour can be considered as analogous to the polarization sensitivity in fluorescence measurements [39, 40] although, for the photoionization case, additional terms - including the photoelectron angular momentum - play a role in determining the modulation depth (sensitivity), and the structure of the PADs [8, 41].

B. Quantum beat spectroscopy: Hyperfine structure

Figure 5 shows Fourier power spectra resulting from the Fourier transform (FT) of the $\beta_L(t)$ (Figure 4). The corresponding feature positions and uncertainties are listed in table I. The FTs of both $\beta_2(t)$ and $\beta_4(t)$ provide the frequency domain parameters $\beta_2(\nu)$ and $\beta_4(\nu)$, associated with both spin-orbit states of the cation. The major features are located around 0.14 cm $^{-1}$ and 0.29 cm $^{-1}$, and minor features around 0.09 cm $^{-1}$ and 0.22 cm $^{-1}$ are observed in some channels. The FT of the photoelectron yields ($\beta_0(\nu)$) reveal very little frequency structure, apart from the lowest frequency feature.

The frequencies listed in table I correspond to the peak of the features observed in the FTs from the major ($J^+ = 3/2$) feature[42], and are reported with uncertainties determined from propagation of the 1σ errors, extracted by analysis of the each scan, as detailed in sect. II B. The statistical uncertainties determined in this manner, on the order of 10^{-3} cm^{-1}, are an order of magnitude better than the absolute frequency limits imposed by the 890 ps temporal window, which corresponds to a lower limit on the observable frequency of $\nu_{min} = 3.75 \times 10^{-2}$ cm^{-1}, and defines the resolution of the FT; this limit is also reflected in the feature widths, which are on the same order as ν_{min}. The statistical uncertainties are, however, significantly worse than the absolute experimental frequency accuracy, which is defined by the timing uncertainty of the measurements: in this case, the pump-probe cross-correlation of the laser pulses, $\tau_{xc} \approx 170$ fs (dispersion limited in the current experiments), which defines a frequency accuracy $\nu_{xc} = 6.2 \times 10^{-6}$ cm^{-1}. The upper limit on the observable frequency is defined by the temporal sampling step size, $\tau_s = 10$ ps, which results in $\nu_{max} = 3.335$ cm^{-1}.

From the measurements, the hyperfine coupling constants can be determined by fitting to the usual form (see, e.g., ref. [18]):

$$\Delta E_{(F,F-1)} = AF + \frac{3}{2}BF\left(\frac{F^2 + \frac{1}{2} - J(J+1) - I(I+1)}{IJ(2J-1)(2I-1)}\right) \quad (2)$$

Where A is the magnetic dipole constant, and B the electric quadrupole constant. Hyperfine constants determined in this manner are reported in table I, and compared with previously reported values. In one case, ^{131}A, the constant is comparable to those previously determined within the experimental uncertainty; in the remaining cases, the constants are comparable to those previously determined, but not within the experimental uncertaintites. This may indicate systematic errors in the experiment and/or data analysis; the presence of electric fields (on the order of 10 - 50 Vcm^{-1} in the present case) in the VMI spectrometer is potentially one source of small shifts (sub-cm^{-1}) on the measured splittings, particularly since the Stark shifts are I and F dependent [43], and a relatively high-lying manifold is accessed. Detailed exploration of this effect remains for future work, although rough estimates on the scale of the effect for Rydberg states can be made from a hydrogenic model [44, 45]. In this model, Stark splitting between adjacent levels is given by $\Delta E_s = 1.28 \times 10^{-4} n\varepsilon$, where ε is the field strength in Vcm^{-1}. This indicates ΔE_s=0.04 cm^{-1} for $n = 6$ and ε=50 Vcm^{-1}, which is significant on the scale of the measured splittings. However, it is of note that previous high-resolution studies of higher n manifolds ($n > 10$), at higher field strengths of $\varepsilon \sim$100 Vcm^{-1}, have neglected such effects [46]. The polarizabilities of

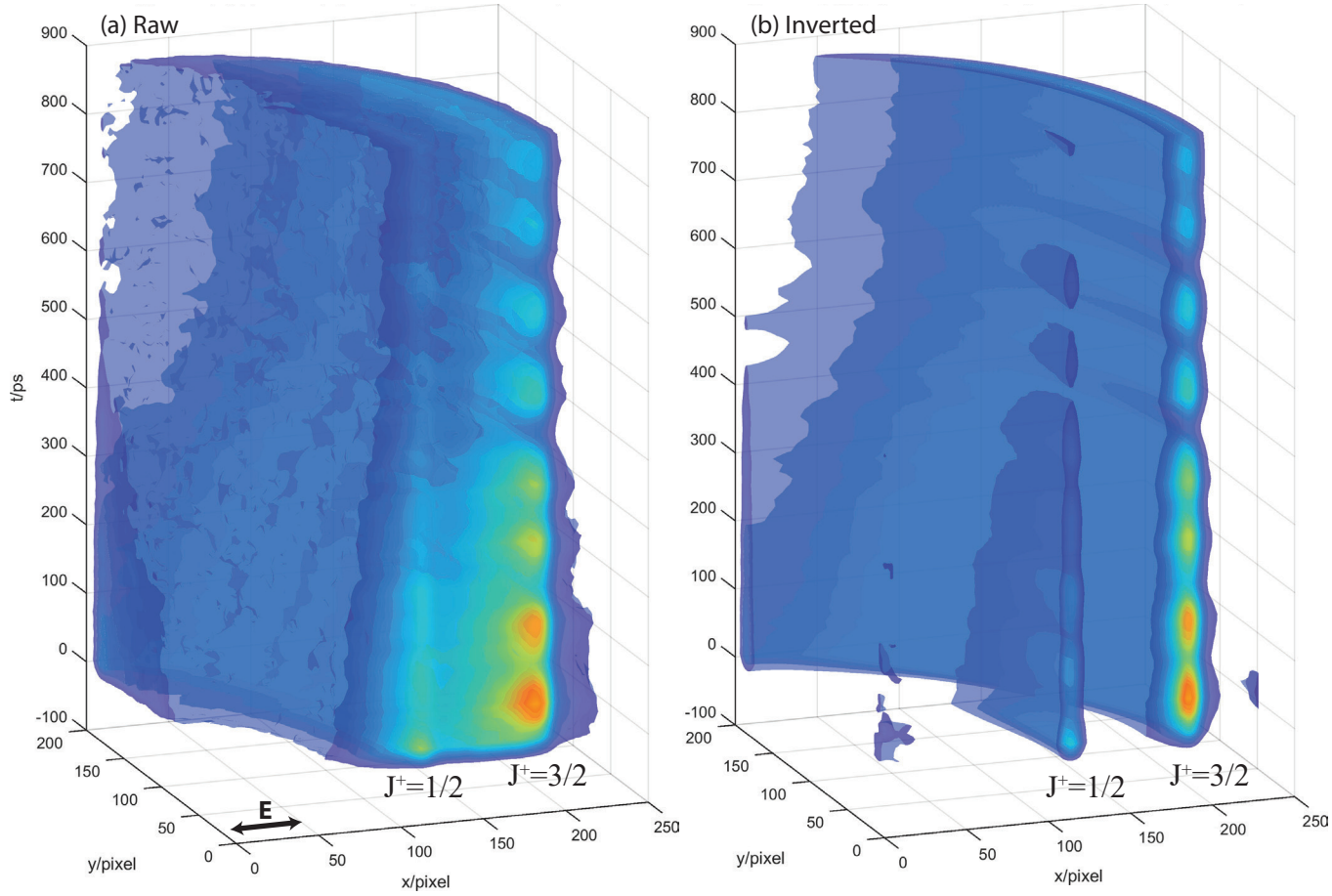

Figure 3. Full image volumes, shown for a single quadrant. (a) Raw data (x, y, t). (b) Inverted images (x_i, y_i, t). Isosurfaces show 10 - 90% photoelectron signal. The full data volume was down-sampled and smoothed for these renderings.

the relevant states in Xe required to calculate ΔE_s accurately [43] are, to the best of our knowledge, not known.

C. Quantum beat imaging

1. *Phenomenology*

For a quantum beat imaging methodology, the full (x, y, t) data volume can be transformed directly to the frequency domain via application of an FT to each pixel. This is a different approach from the treatment of the $\beta_L(t)$ parameters detailed above, since it does not require inversion of the raw image stack, hence is directly applicable even in the case of complex, non-invertable images (see Sect. II B). The resulting (x, y, ν) images provide the Fourier components of the time-resolved photoelectron images.[49] In cases where inversion is applicable, the processed data volume (x_i, y_i, t) can be similarly transformed.

In the present case, the frequency components correspond to the hyperfine level splittings, and there is separation of the $I = 0$ isotopes from the $I \neq 0$ isotopes in the frequency-domain, since only the latter can contribute to the time-dependence of the signal (i.e. $\nu > 0$), while the former will only contribute to the time-independent (DC) part of the signal (i.e. $\nu = 0$). Furthermore, if the Fourier components are uniquely associated with a particular isotope, then different frequency-domain images will correspond to isotopically-resolved wavepacket components and associated frequency-domain photoelectron images. For this assertion to be valid, the isotope signals must be incoherent, and the level-splittings must be resolved in the frequency-domain. If these conditions hold, then the Fourier components provide a means to obtain isotopically-resolved photoelectron distributions, correlated with pairs of hyperfine states. (This is conceptually similar to the recent photoelectron-photoion coincidence measurements mentioned previously [21, 22], except that the information obtained is a set of Fourier image components from a dynamical system, rather than state resolved photoelectron distributions.)

Figures 6 and 7 illustrate the Fourier domain images (absolute values). The main discrete frequency compo-

Isotope	F, F'	Splitting/cm^{-1}	Hyperfine consts.		Literature	
			A/MHz	B/MHz	A/MHz	B/MHz
129 ($I = 1/2$)	1/2, 3/2	0.2863 (5)	-5723 (9)	-	-5808 (2) [a], -5806 (4) [b], -5799 (9) [c]	-
131 ($I = 3/2$)	3/2, 1/2	0.0855 (10)	1697 (30)	-8 (7)	1709.3 (7) [a], 1710 (6) [b], 1716 (3) [c]	30.3 (8) [a], 16 (3) [b], 24 (6) [c]
	5/2, 3/2	0.1411 (29)				
	5/2, 1/2	0.2276 (29)				

Table I. Measured level splittings and the hyperfine constants determined. Statistical uncertainty estimates are given for the measurements. Literature values reproduced from ref. [18], table II, with [a] D'Amico et. al. (1999) [18], [b] Jackson & Coulombe (1972) [47], [c] Fischer et. al. (1974) [48].

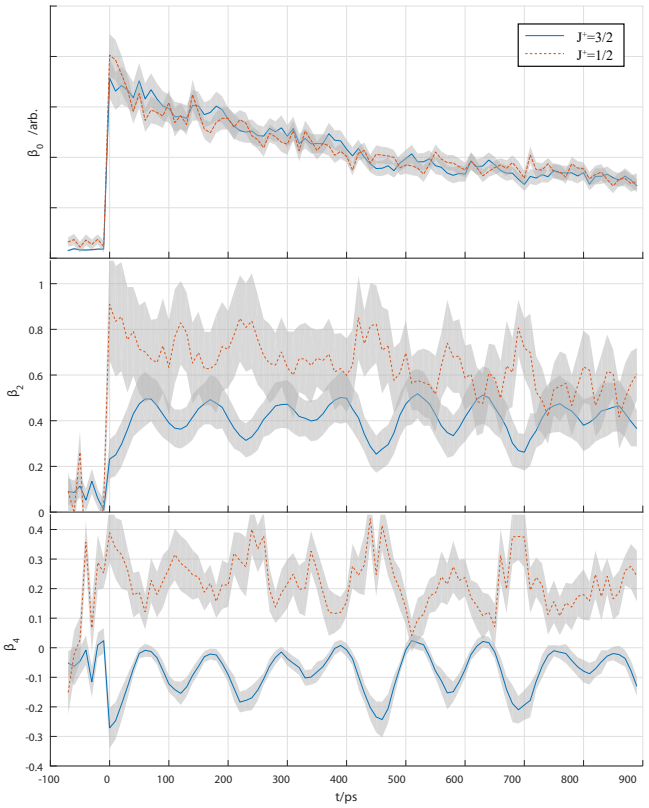

Figure 4. Time-dependent $\beta_L(t)$ parameters, $J^+ = 3/2$ (blue, solid), $J^+ = 1/2$ (orange, dashed). Uncertainties show statistical errors (1σ), determined from analysis of each experimental cycle - see Sect. II B for details.

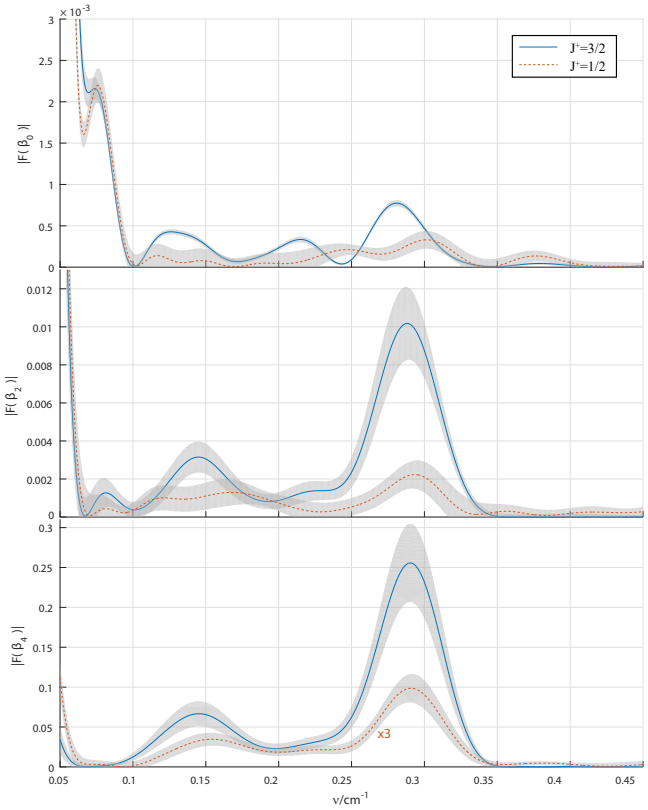

Figure 5. Frequency domain results $\beta_L(\nu)$, obtained via Fourier transform of the $\beta_L(t)$ data shown in fig. 4. Plots show the Fourier power spectrum for each trace, with statistical uncertainties (1σ), determined from analysis of each experimental cycle - see sect. II B for details.

nents, correlated with the level splittings given in table I, are shown in Figure 6; Figure 7 provides renderings of the full frequency domain image volumes. A number of phenomenological observations may be made from these results.

In both sets of images, the angular features are peaked along the laser polarization axis (x-axis, corresponding to positive β_2), and this appears to be the dominant contribution in all cases. In terms of the hyperfine wavepacket, the images correlate with beat frequencies, hence pairs of F levels. The photoelectron interference pattern for each pair therefore contains two contributions [50]:

1. the "intrinsic" photoionization interferences, due to the partial-wave composition of the continuum wavefunction, which would be observed for ionization of a single (eigen)state;

2. additional interferences which arise in the sum over pairs of F states, and include a time-dependence due to the time-evolution of the prepared wavepacket.

In the case of ^{131}Xe, there is an additional layer of complexity, since there are multiple F pairs which contribute to the final photoelectron images. In these results, it appears that interferences between the components[51] at

0.09 and 0.14 cm^{-1} - which have lobes with different angular spreads (see fig. 6) - is the main source of the $\beta_4(t)$ oscillations observed (Figs. 4 & 5); this is also consistent with the lack of a $\beta_4(\nu)$ feature at 0.09 cm^{-1} (Fig. 5). In contrast, for ^{129}Xe only a single Fourier image component is present (0.29 cm^{-1}), indicating that any $\beta_4(t)$ oscillations correlated with this isotope originate from just this F pair; this is consistent with the significant $\beta_4(\nu)$ feature observed at this frequency (fig. 5). This is also suggested by the greater angular complexity in the images (higher L terms), as compared to the ^{131}Xe images. This is observed most clearly in the inverted image, which contains multiple lobes for both spectral features. Of note here is the fact that, in the Fourier domain images, higher order angular patterns than usually allowed for a 2-photon process ($L_{max} = 4$) can appear due to the differential nature of the images. The images in this case therefore indicate that the intrinsic ionization dynamics of the two F states involved would result in different four-fold distributions. However, quantitative analysis along these lines requires knowledge of the photoionization matrix elements, either from calculation or via retrieval from experimental data. In the latter case, previous work has shown that this may be possible for hyperfine wavepacket data [50, 52, 53], and the data obtained in this work may also contain sufficient information for such a retrieval. Work is ongoing in this direction, and some general comments are presented in the following section.

Another interesting feature of the images presented in fig. 6 is the absence of any appreciable intensity in the inner ring for the images correlated with 0.14 cm^{-1} and 0.23 cm^{-1}. This indicates very little population of the $J^+ = 1/2$ state of the cation via ionization from these components of the hyperfine wavepacket. Finally, it is interesting to note that the widths (radial spread) of the features is not constant. This is seen most clearly in the inverted image volumes of fig. 7, but is also apparent in the inverted images of fig. 6. In particular, the 0.29 cm^{-1} feature has a larger radial extent that the 0.14 cm^{-1} feature, indicating slight changes in the photoelectron energy spectra associated with these components.

2. *Phase imaging and wavepacket treatment*

In the preceeding discussion, the QB imaging results were presented along with a basic phenomenological discussion. Further insight into the results can be obtained via the associated phase structure of the (x, y, ν) data. Fig. 8 shows the phase images for the observed features, for both the raw and inverted images, corresponding to the absolute value images shown in fig. 6. Broadly speaking, the phase structure is similar for both the raw and inverted images, indicating the possibility of accessing phase information directly from the raw image stacks as suggested previously. Unsurprisingly, the inverted images contain a clearer and more pronounced phase structure[54]. This occurs simply because the photoelectron features do not overlap in the inverted (slice) images, which show clear rings and associated phases, in contrast to the raw (crush) images, which show continuous phase structure over the images.

Exploration of the phase structure in the images provides an alternative analysis methodology, which can be compared with many of the observations previously discussed. For instance, the inner and outer photoelectron bands are out-of-phase; this effect is particularly clear in the 0.14 and 0.29 cm^{-1} features, and is in agreement with the phase shift observed in the $\beta_L(t)$ plots pertaining to the two different final states (fig. 4). The appearance of additional angular structure in the 0.29 cm^{-1} feature, discussed in the previous section as a result of different final continuum states related to each ionizing F state, is now made clearer by the alternating phase pattern in the outer ring. This phase structure indicates the phase difference between the two F state contributions, with the equatorial region shifted from the four-fold lobe structure by just over π radians. This phase structure quantitatively maps the change in angular structure as a function of t observed in the original time-domain images (fig. 2).

A formal statement of the phase contributions can be obtained from a wavepacket treatment, in which the full complexity of the photoionization dynamics remains implicit. In general, the signal for a PAD measured by one-photon ionization with linearly polarized light from a wavepacket can be written as

$$I(\theta, E, t) \propto |\langle \Psi(t) | \mu_Z | \Phi_f^+ \psi_e(E, \theta) \rangle|^2. \tag{3}$$

Here $\Psi(t)$ is the bound wavepacket, μ_Z is the dipole moment along the polarization direction of the light, Φ_f^+ and $\psi_e(E, \theta)$ are the final ionic state and photoelectron wavefunctions respectively. To begin with assume that the wavepacket is a superposition of two hyperfine components,

$$\Psi(t) = c_1 e^{iE_1/\hbar t} |F_1\rangle + c_2 e^{iE_2/\hbar t} |F_2\rangle . \tag{4}$$

where c_i and E_i are the coefficients and energies of the hyperfine states. Inserting this into into Eq. 3 and expanding gives,

$$\begin{aligned} I(\theta, E, t) = {} & P_1 |d_1^f|^2 + P_2 |d_2^f|^2 \\ & + c_1^* c_2 d_1^f d_2^{f*} e^{i\Omega t} + c_1 c_2^* d_1^{f*} d_2^f e^{-i\Omega t}. \end{aligned} \tag{5}$$

$P_1 = |c_1|^2$ and $P_2 = |c_2|^2$ are the populations of the two hyperfine states. $d_1^f = \langle F_1 | \mu_Z | \Phi_f^+ \psi_e(E, \theta) \rangle$ is the ionization dipole matrix out of the F_1 state, and d_2^f is the same out of F_2. The dependence of these on E and θ is implicit. $\Omega = (E_2 - E1)/\hbar$ is the angular beat frequency between the hyperfine states. Note that the last two terms in the above expression are conjugates. As a result, if the dipole matrix elements and wavepacket coefficients

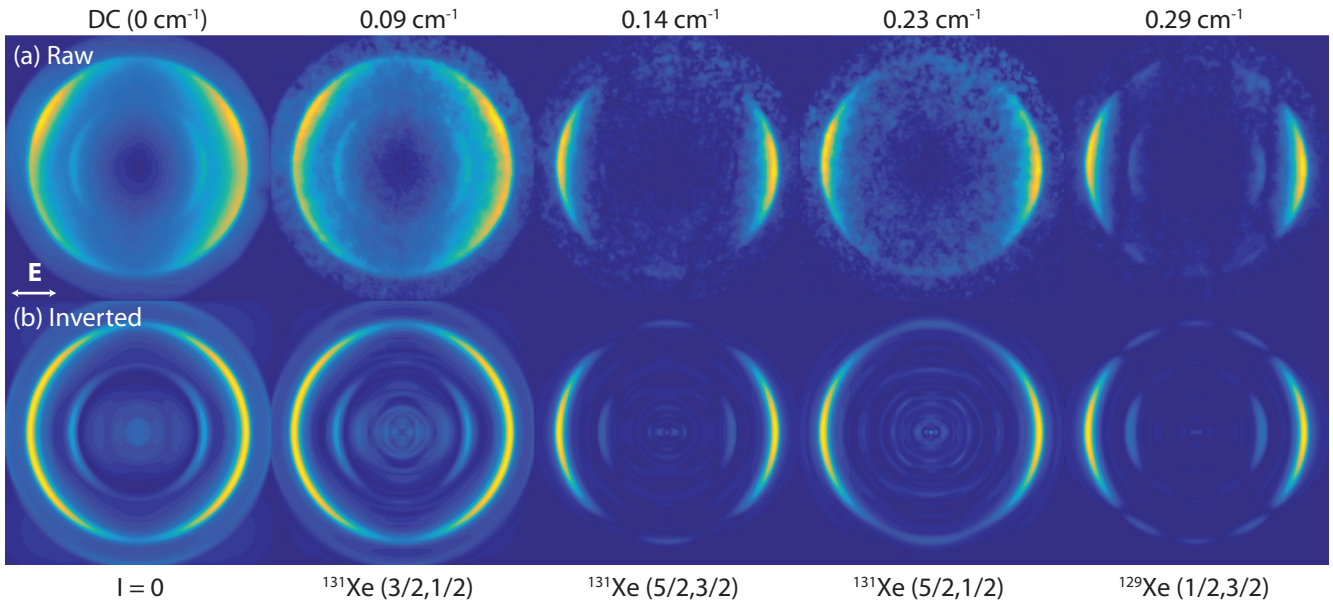

Figure 6. Fourier image components (absolute value) corresponding to the observed features (see fig. 5 and table I). (a) FT images from the raw image stack. (b) FT images from the inverted image stack. Full image stacks are shown in fig. 7. Colour maps were normalised independently for each image.

are expressed in terms of their amplitudes and phases, the following expression results -

$$I(\theta,E,t) = P_1|d_1^f|^2 + P_2|d_2^f|^2 + 2|c_1||c_2||d_1^f||d_2^f|\cos\left[\Omega t + \Delta\phi^c_{1,2} + \Delta\phi^f_{1,2}\right] \quad (6)$$

From this expression the images obtained by the FT of $I(\theta,E,t)$ can be understood.

The $I(\theta,E,\nu=0)$ image corresponding to the DC component of the FT is given by $P_1|d_1^f|^2 + P_2|d_2^f|^2$. The angle and energy dependent structure in these images is therefore entirely determined by the magnitudes of the ionization dipoles out of each component states. The contribution of each component state is determined by their populations. These images will have only a real component, and reflect the "intrinsic" photoionization dynamics, hence the sum over the corresponding PADs from each component state.

The $I(\theta,E,\nu)$ images corresponding to the beat frequencies on the other hand should have an amplitude and phase. The structure in the amplitude image is determined by the product of the ionization dipoles - $|d_1^f(E,\theta)||d_2^f(E,\theta)|$ - and that of the phase image by the phase difference between the ionization dipoles - $\Delta\phi^f_{1,2}(E,\theta)$. Note both the amplitude and phase are offset by constants determined by the product of the magnitudes of the wavepacket coefficients, and their phase differences ($\Delta\phi^c_{1,2}$) respectively. As such these images represent a direct measurement of the interfering ionization pathways out of the component states of the wavepacket.

Eq 6 can be easily generalized to a wavepacket of N component eigenstates -

$$I(\theta,E,t) = \sum_i P_i|d_i^f|^2 + \sum_{j<k} 2|c_j||c_k||d_j^f||d_k^f| \times \cos\left[\Omega t + \Delta\phi^c_{j,k} + \Delta\phi^f_{j,k}\right]. \quad (7)$$

The indicies i,j and k run over all N states. Thus in the case where numerous eigenstates compose the wavepacket, the FT images for each beat frequency separate out the interference patterns resulting from ionization from each pair of states.

IV. CONCLUSIONS AND FUTURE WORK

In this work, the combination of a 130 nm VUV source with a pump-probe methodology and photoelectron imaging measurements has been demonstrated, and used to probe a hyperfine wavepacket in Xe. The measurement of images over a large time-window, and with high timing accuracy, provided hyperfine splittings and coupling constants which were compared with literature values. The full imaging data was also investigated in the frequency domain, and the retrieval of images correlated with different isotopes and wavepacket components, via FT of the image volume, was demonstrated and explored.

From a QBS perspective, the use of a fs VUV source (ideally tuneable), combined with a UV ionization probe, provides a method applicable to a range of systems, and

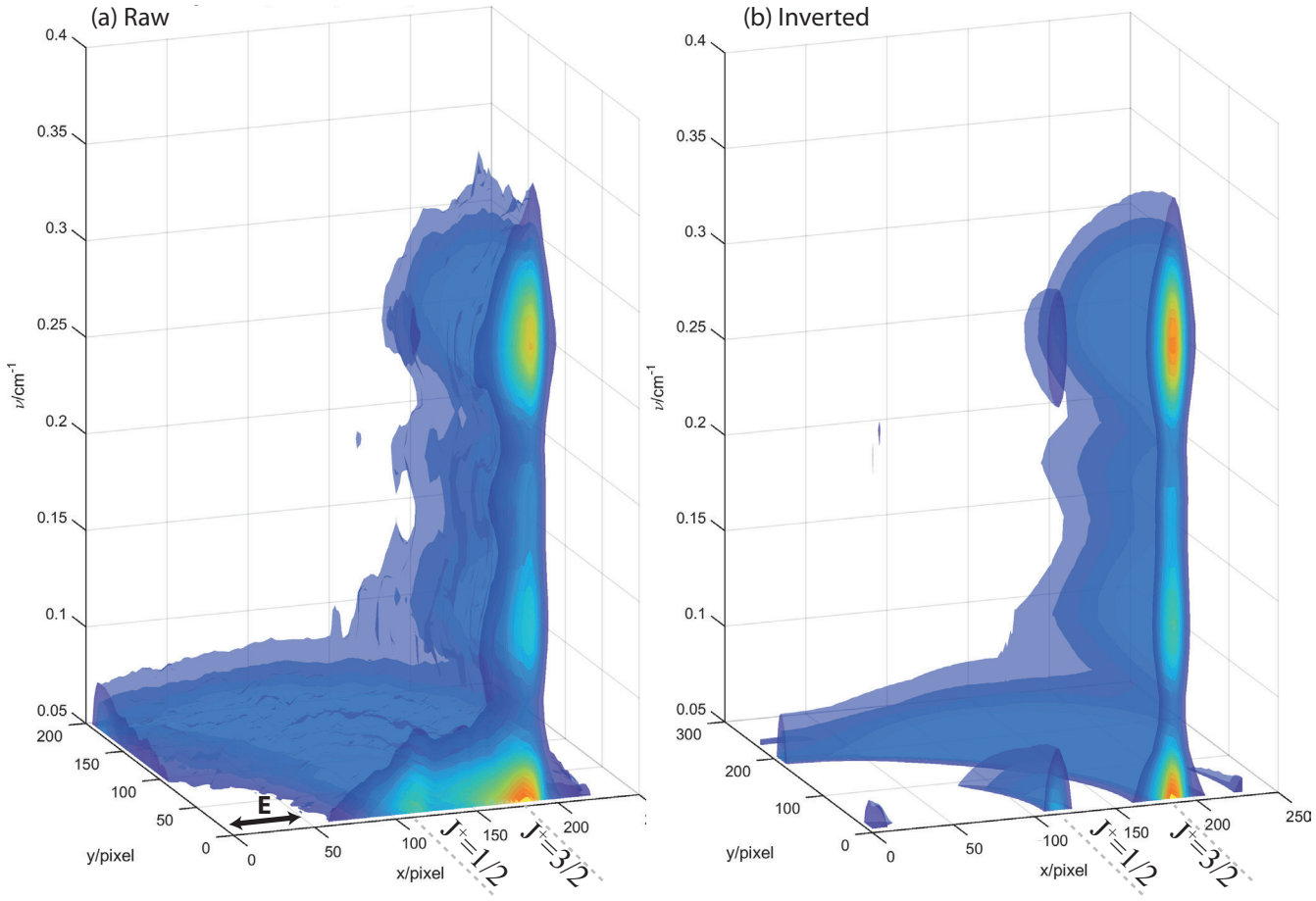

Figure 7. Fourier image volumes (absolute values, single quadrant). (a) FT of the raw image stack (x, y, ν). (b) FT of the inverted image stack (x_i, y_i, ν). Isosurfaces show 10 - 90% photoelectron signal. The full data volume was down-sampled and smoothed for these renderings. The main features correspond to the images shown in fig. 6.

which can be used to interrogate high-lying manifolds which are typically hard to access [55]. As discussed in ref. [56], "in view of the paucity of the data measured so far and because of the possibility of carrying out accurate calculations, PADs from excited states of the heavier rare-gas atoms offer an interesting opportunity for combined experimental and theoretical studies in the future"; the authors also mention that "PAD studies involving selected excited states of the rare-gas atoms are also scarce", as are studies of auto-ionizing states. Ultrafast pump-probe VUV-UV measurements certainly provide a technique suitable for investigating this area, and the broadband laser pulses are also suitable for cases with larger level splittings, hence QBS of lighter elements. For an extended discussion of recent developments in precision laser spectroscopies in the VUV and XUV, see ref. [27]. For short pulses, limitations on frequency resolution are placed, effectively, only by the temporal sampling parameters of the measurements. The difficulty of such measurements lies, instead, in the lengthy experimental runs that may be required for very high-precision measurements, and consequent requirements for long-term experimental stability. The ability to extract frequency-correlated images is a novel emergent property of time-resolved photoelectron imaging experiments with sufficient spatio-temporal sampling (data volume), and one which allows for beat-component and isotope-correlated imaging in favourable cases, as demonstrated herein.

From a more general time-domain spectroscopy perspective, the results presented herein are a subset of wavepacket measurements. In this vein, there is a significant literature on time-resolved photoelectron spectroscopy and imaging, PADs and related work (see, for instance, ref. [57] for a basic introduction, and refs. [58–64] for further discussion and review). Despite this extant work, a Fourier transform photoelectron imaging methodology has not previously been explored, to the best of our knowledge. Since the analysis methodology is somewhat obvious, in the sense that it is a clear extension of standard (but lower dimensionality) time-domain analyses, this is presumably due to the lack of sufficient data volumes in other cases. Many factors may contribute here, including the native time-scale and complexity of the process under study, the experimental difficulty of ob-

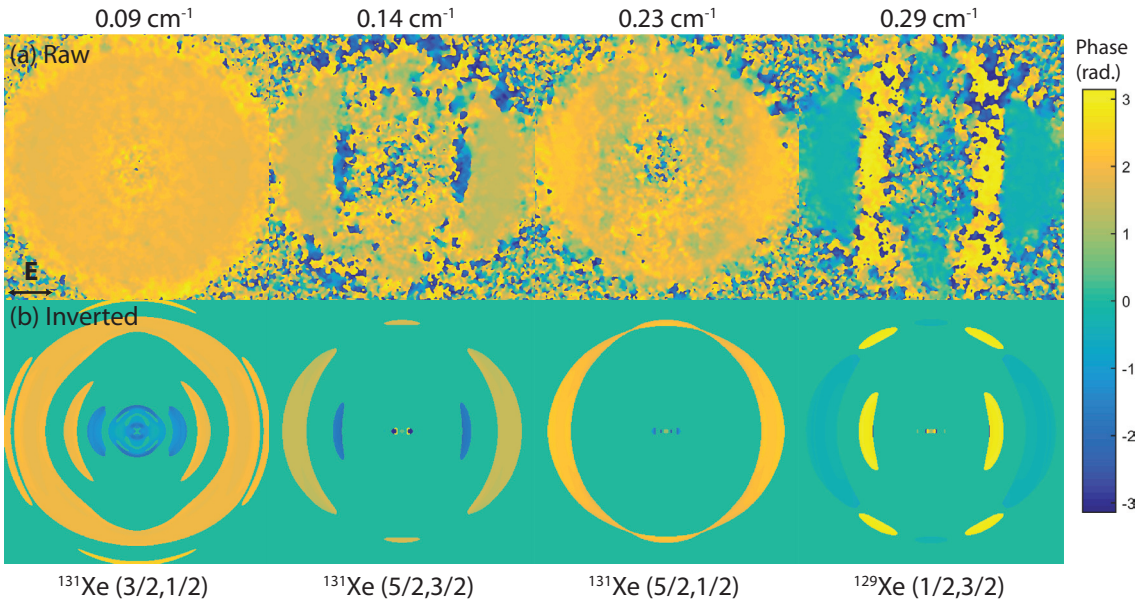

Figure 8. Fourier image components (phases) corresponding to the observed features (see fig. 5 and table I). (a) FT images from the raw image stack. (b) FT images from the inverted image stack. The corresponding absolute value images are presented in fig. 6.

taining sufficient measurements, or additional sampling constraints. Despite these challenges, the ability to obtain some phase information directly from the raw images is, potentially, an interesting feature of this type of analysis and may motivate future studies.

Apart from the image processing, and determination of the hyperfine coupling constants, the analysis presented herein is relatively phenomenological. As mentioned above, future work will aim to address this point by consideration of both the hyperfine wavepacket and photoionization dynamics in more detail, making use of the formalism developed by Berry and coworkers [50]. Such investigation is, necessarily, rather involved, but would provide a more detailed insight into the import of the FT images presented herein, and the information content of the quantum beat imaging methodology. In the case of a sufficiently high information content, it is possible that the full photoionization dynamics and wavepacket dynamics could be retrieved/reconstructed from the experimental data - this is a form of "complete" experiment in photoionization terminology, and can also be considered as a form of quantum metrology or tomography in the language of quantum information [63–65].

V. ACKNOWLEDGEMENTS

We are grateful to Andrey Boguslavskiy, Denis Guay and Doug Moffat for assistance with the experimental infrastructure, and technical support. AS thanks the NSERC Discovery Grant program for financial support.

VI. SUPPLEMENTARY MATERIAL

Raw data, processing routines and additional analysis documentation are available via an online OSF repository, **Quantum Beat Photoelectron Imaging Spectroscopy of Xe in the VUV**, DOI: 10.17605/OSF.IO/DS8MK. This repository provides a complete reporting of the analysis routines (Matlab scripts), including full details of the image processing and Fourier transform routines (which included zero-padding and a Hann window function in the results shown herein), for readers who wish to explore the technique in further detail or build on the code-base developed.

[1] S. Haroche, J. A. Paisner, and A. L. Schawlow, Physical Review Letters **30**, 948 (1973).

[2] D. J. Tannor, *Introduction to quantum mechanics : a time-dependent perspective* (Univ. Science Books, 2007).

[3] E. Hack and J. R. Huber, International Reviews in Physical Chemistry **10**, 287 (1991).

[4] K. Blum, *Density Matrix Theory and Applications* (Springer US, 1996).

[5] E. Arimondo, M. Inguscio, and P. Violino, Reviews of Modern Physics **49**, 31 (1977).

[6] M. P. Strand, J. Hansen, R.-L. Chien, and R. Berry, Chemical Physics Letters **59**, 205 (1978).

[7] J. C. Hansen, J. A. Duncanson, R.-L. Chien, and R. S. Berry, Physical Review A **21**, 222 (1980).

[8] R. ling Chien, O. C. Mullins, and R. S. Berry, Physical Review A **28**, 2078 (1983).

[9] C. H. Greene and R. N. Zare, Physical Review A **25**, 2031 (1982).

[10] H. Klar and H. Kleinpoppen, Journal of Physics B: Atomic and Molecular Physics **15**, 933 (1982).

[11] S. J. Bajic, R. N. Compton, X. Tang, and P. Lambropoulos, Physical Review A **44**, 2102 (1991).

[12] K. L. Reid, S. P. Duxon, and M. Towrie, Chemical Physics Letters **228**, 351 (1994).

[13] T. Meier, H. Hühnermann, and H. Wagner, Optics Communications **20**, 397 (1977).

[14] P. Cahuzac and R. Vetter, Physical Review Letters **34**, 1070 (1975).

[15] F. Brandi, I. Velchev, W. Hogervorst, and W. Ubachs, Physical Review A **64** (2001), 10.1103/physreva.64.032505.

[16] T. A. Paul and F. Merkt, Journal of Physics B: Atomic Molecular and Optical Physics **38**, 4145 (2005).

[17] H. J. Wörner, M. Grütter, E. Vliegen, and F. Merkt, Physical Review A **71** (2005), 10.1103/physreva.71.052504.

[18] G. D'Amico, G. Pesce, and A. Sasso, Physical Review A **60**, 4409 (1999).

[19] M. Schäfer, M. Raunhardt, and F. Merkt, Physical Review A **81** (2010), 10.1103/physreva.81.032514.

[20] V. L. Sukhorukov, I. D. Petrov, M. Schäfer, F. Merkt, M.-W. Ruf, and H. Hotop, Journal of Physics B: Atomic, Molecular and Optical Physics **45**, 092001 (2012).

[21] P. O'Keeffe, E. V. Gryzlova, D. Cubaynes, G. A. Garcia, L. Nahon, A. N. Grum-Grzhimailo, and M. Meyer, Physical Review Letters **111** (2013), 10.1103/physrevlett.111.243002.

[22] E. V. Gryzlova, P. O'Keeffe, D. Cubaynes, G. A. Garcia, L. Nahon, A. N. Grum-Grzhimailo, and M. Meyer, New Journal of Physics **17**, 043054 (2015).

[23] In Racah notation, where the core is given by the term symbol $(^{2S+1}L_J)$ and the excited electron is defined by $nl\ ^{2S+1}[K]_{J_e}$, where $K = J + l$ and $J_e = K + s$.

[24] A. Kramida, Y. Ralchenko, J. Reader, and N. A. Team, "NIST Atomic Spectra Database (version 5.5.2)," (2018).

[25] R. Forbes, V. Makhija, K. Veyrinas, A. Stolow, J. W. L. Lee, M. Burt, M. Brouard, C. Vallance, I. Wilkinson, R. Lausten, and P. Hockett, The Journal of Chemical Physics **147**, 013911 (2017).

[26] T. Suzuki, Journal of Physics B: Atomic Molecular and Optical Physics **47**, 124001 (2014).

[27] K. S. Eikema and W. Ubachs, in *Handbook of High-resolution Spectroscopy* (John Wiley & Sons, Ltd, Chichester, UK, 2011).

[28] P. Trabs, *Generation and utilization of femtosecond light pulses in the vacuum-ultraviolet spectral regime (PhD thesis)*, Ph.D. thesis, Freien Universität Berlin (2015), accessed on Thu, February 22, 2018.

[29] P. Trabs, H.-H. Ritze, and F. Noack, in *Conference on Lasers and Electro-Optics* (OSA, 2016).

[30] A. T. J. B. Eppink and D. H. Parker, Review of Scientific Instruments **68**, 3477 (1997).

[31] U. Even, J. Jortner, D. Noy, N. Lavie, and C. Cossart-Magos, The Journal of Chemical Physics **112**, 8068 (2000).

[32] K. L. Reid, Annual Review of Physical Chemistry **54**, 397 (2003).

[33] B. J. Whitaker, ed., *Imaging in Molecular Dynamics* (Cambridge University Press, 2003).

[34] G. A. Garcia, L. Nahon, and I. Powis, Review of Scientific Instruments **75**, 4989 (2004).

[35] P. Hockett, C. Lux, M. Wollenhaupt, and T. Baumert, Physical Review A **92** (2015), 10.1103/physreva.92.013412.

[36] R. D. Knight and L. guo Wang, Journal of the Optical Society of America B **2**, 1084 (1985).

[37] F. Brandi, I. Velchev, W. Hogervorst, and W. Ubachs, Physical Review A **64** (2001), 10.1103/physreva.64.032505.

[38] K. L. Reid, S. P. Duxon, and M. Towrie, Chemical Physics Letters **228**, 351 (1994).

[39] S. Haroche, J. A. Paisner, and A. L. Schawlow, Physical Review Letters **30**, 948 (1973).

[40] U. Fano and J. H. Macek, Reviews of Modern Physics **45**, 553 (1973).

[41] H. Klar and H. Kleinpoppen, Journal of Physics B: Atomic and Molecular Physics **15**, 933 (1982).

[42] Slight shifts in the features for the minor channel ($J^+ = 1/2$) were observed in some cases, and the statistical uncertainties were significantly larger. Both effects were attributed to the worse signal-to-noise for the minor feature (see figure 4).

[43] J. R. P. Angel and P. G. H. Sandars, Proceedings of the Royal Society A: Mathematical Physical and Engineering Sciences **305**, 125 (1968).

[44] M. L. Zimmerman, M. G. Littman, M. M. Kash, and D. Kleppner, Physical Review A **20**, 2251 (1979).

[45] W. A. Chupka, The Journal of Chemical Physics **98**, 4520 (1993).

[46] M. Kono, Y. He, K. G. H. Baldwin, and B. J. Orr, Journal of Physics B: Atomic Molecular and Optical Physics **46**, 035401 (2013).

[47] D. A. Jackson and M. C. Coulombe, Proceedings of the Royal Society A: Mathematical Physical and Engineering Sciences **327**, 137 (1972).

[48] W. Fischer, H. Hühnermann, G. Krömer, and H. J. Schäfer, Zeitschrift für Physik **270**, 113 (1974).

[49] By analogy with other imaging techniques, this can also be termed "hyperspectral.

[50] R. ling Chien, O. C. Mullins, and R. S. Berry, Physical Review A **28**, 2078 (1983).
[51] More precisely, between the underlying photoelectron wavefunctions correlated with each of the three F states involved.
[52] M. P. Strand, J. Hansen, R.-L. Chien, and R. Berry, Chemical Physics Letters **59**, 205 (1978).
[53] J. C. Hansen, J. A. Duncanson, R.-L. Chien, and R. S. Berry, Physical Review A **21**, 222 (1980).
[54] It is of note here that the inverted phase images include an intensity mask, with a threshold at ≈5% of the photoelectron yield, to remove spurious phase noise in energy regions with no signal.
[55] T. A. Paul and F. Merkt, Journal of Physics B: Atomic Molecular and Optical Physics **38**, 4145 (2005).
[56] V. L. Sukhorukov, I. D. Petrov, M. Schäfer, F. Merkt, M.-W. Ruf, and H. Hotop, Journal of Physics B: Atomic, Molecular and Optical Physics **45**, 092001 (2012).
[57] G. Wu, P. Hockett, and A. Stolow, Physical Chemistry Chemical Physics **13**, 18447 (2011).
[58] T. Suzuki and B. J. Whitaker, International Reviews in Physical Chemistry **20**, 313 (2001).
[59] T. Seideman, Physical Review A **64** (2001), 10.1103/physreva.64.042504.
[60] T. Suzuki, Annual Review of Physical Chemistry **57**, 555 (2006).
[61] A. Stolow and J. G. Underwood, in *Advances in Chemical Physics* (John Wiley & Sons Inc., 2008) pp. 497–584.
[62] K. L. Reid, Molecular Physics **110**, 131 (2012).
[63] P. Hockett, *Quantum Metrology with Photoelectrons, Volume 1: Foundations* (Morgan & Claypool, for IOP Concise Physics, 2018).
[64] P. Hockett, *Quantum Metrology with Photoelectrons, Volume 2: Applications and Advances* (Morgan & Claypool, for IOP Concise Physics, 2018).
[65] H. Kleinpoppen, B. Lohmann, and A. N. Grum-Grzhimailo, *Perfect/Complete Scattering Experiments* (Springer Berlin Heidelberg, 2013).